

Carrier Diffusion Lengths in Hybrid Perovskites: Processing, Composition, Aging, and Surface Passivation Effects

Gede W. P. Adhyaksa,[†] Leon W. Veldhuizen,[‡] Yinghuan Kuang,[‡] Sarah Brittman,[†] Ruud E. I. Schropp,[‡] and Erik C. Garnett^{*,†}

[†]Center for Nanophotonics, FOM Institute AMOLF, Science Park 104, 1098 XG Amsterdam, The Netherlands

[‡]Department of Applied Physics, Plasma & Materials Processing, Eindhoven University of Technology, P.O. Box 513, 5600 MB Eindhoven, The Netherlands

S Supporting Information

Hybrid halide perovskites are an emerging class of semiconductors that has drawn great interest recently because of its simple solution processing, tunable band gap, high solar cell efficiency, and low lasing threshold.^{1–5} They have the same ABX₃ configuration as the classic oxide perovskites but have metal halide rather than metal oxide corner-sharing octahedra. Typically, organic cation A is methylammonium (MA) or formamidinium (FA), B is lead (Pb) or tin (Sn), and X is chloride (Cl), bromide (Br), or iodide (I); already combining just these ions in pure or 50/50 mixes, nearly 50 distinct varieties emerge. Such compositional variations strongly affect material properties. For example, the addition of only a few percent of PbCl₂ to MAPbI₃ (so-called MAPbI_{3-x}Cl_x) increases the film's diffusion length from ~100 nm to ~1 μm and raises optimized photovoltaic efficiency from 4.2% to 12.2%.⁶ Even within a single material composition, solvent engineering used to increase the grain size of the film has already been shown to have dramatic effects on device performance.^{3,7} While there are many ways to screen materials and processing conditions, the diffusion length of the photogenerated carrier has been one of the properties most strongly correlated with optoelectronic device performance.^{6,8}

Despite this importance, the most common methods for measuring this diffusion length are not compatible with simple, rapid screening that would be ideal for testing the large number of possible new materials and processing conditions. For example, photoluminescence lifetime measurements can be combined with mobility measurements to yield indirectly the carrier diffusion length, but these measurements are impractically slow to be used for routine testing. Clearly a simple, rapid, and direct method for measuring diffusion length would be useful in screening both new hybrid halide perovskite materials and processing conditions that lead to better material quality.

Here we apply such a method, called the steady-state photocarrier grating (SSPG) technique, to hybrid perovskite materials and use it to investigate the influence of material composition, material processing conditions, aging, and surface passivation on the diffusion length. Originally developed in the 1980s as a way to measure diffusion length in amorphous silicon thin films, SSPG relies on a change in conductivity in the presence of an optical grating created by two interfering laser beams.^{9,10} First, we use SSPG to show that varying the solvent and processing conditions can lead to at least a factor of 2 variation in the diffusion length of methylammonium lead iodide (MAPbI₃). Next we demonstrate how the diffusion

length varies with halide substitution, and for each composition, how it changes with aging. Finally, we show that a thin (4 nm) passivating aluminum oxide layer can increase the diffusion length of methylammonium lead bromide (MAPbBr₃) by nearly a factor of 3, while the process of adding the same coating dramatically degrades MAPbI₃.

Figure 1a shows a schematic of our SSPG measurement setup, where we measure a small change in sample conductivity (at a given voltage) in the presence of an optical grating. The optical grating is created by overlapping two interfering laser beams on the sample. The measurement is conducted under illumination of *I*₁ and *I*₂, where the intensity of beam *I*₁ is much stronger than the chopped beam *I*₂. In this way, *I*₁ serves as a background illumination ensuring an almost constant carrier generation rate over the sample surface, while *I*₂ acts as a probe beam providing a small perturbation (~5%). The change in conductivity is directly measured on the sample using a lock-in amplifier for two configurations: (1) when the two beams have orthogonal polarization states and therefore do not interfere (Figure 1b), and (2) when the polarization states are aligned, creating a periodic optical grating (Figure 1c). The grating period can be controlled by changing the angle between the two beams (grating period decreases as angle increases). The down-transport mirrors, up-transport mirrors, and rotating stages enable continuous overlap between *I*₁ and *I*₂ with varying angle.

Solving the one-dimensional steady-state diffusion equation leads to a relation between the photoconductivity ratio and grating period:^{11–13}

$$\left(\frac{1}{1-\beta}\right)^{1/2} = \frac{(2\pi L_D)^2}{(2Z)^{1/2}} \left(\frac{1}{\Lambda}\right)^2 + \frac{1}{(2Z)^{1/2}} \quad (1)$$

where Λ is the grating period, β is the photoconductivity ratio of lock-in amplifier signals under the parallel and perpendicular polarization configurations (Figure 1c,b), L_D is the diffusion length of the photogenerated carrier, and Z is a fitting parameter related to nonideal grating formation (e.g., due to surface scattering or poor photoconductivity). L_D describes ambipolar transport of the Coulomb-coupled electron and hole, but it will be dominated by the photogenerated carrier with the

Received: February 1, 2016

Revised: July 19, 2016

Published: July 25, 2016

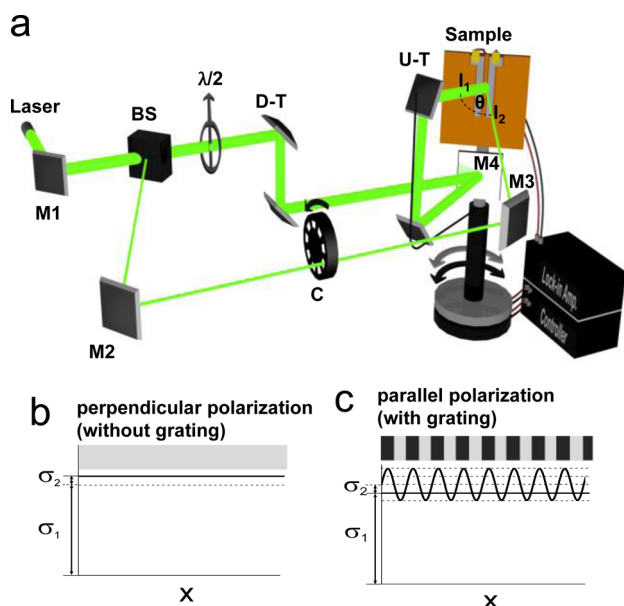


Figure 1. (a) Schematic of the setup: I_1 is the strong beam, I_2 is the weak beam, θ is the angle between I_1 and I_2 , M_1 , M_2 , M_3 , and M_4 are mirrors, BS is a beam splitter, $\lambda/2$ is a half-wave plate, C is a chopper, $U-T$ are up-transport mirrors, and $D-T$ are down-transport mirrors. The axis has two rotating stages (black and gray) and each can rotate independently: (1) the sample along with M_4 underneath (gray arrow) and (2) the up-transport mirrors connected with the arm (black arrow). Sample: a perovskite film deposited on a glass substrate with two coplanar gold electrodes. (b) Lateral conductivity pattern without grating: when I_1 and I_2 are orthogonally polarized. (c) Lateral conductivity with grating: when I_1 and I_2 are in parallel polarization. The conductivity σ_1 and σ_2 are not to scale for better visualization (perturbation by σ_2 should be very small relative to σ_1 in order to maintain the steady-state condition).

smaller diffusion length (e.g., minority carrier in a doped material). The value of β will be close to unity when the diffusion length is much longer than the grating period. This case takes place when carrier diffusion significantly smears out the grating, so that the signal is the same if I_1 and I_2 create a grating (Figure 1c) or not (Figure 1b). Increasing the grating period beyond the diffusion length drastically decreases the sample conductivity, consequently decreasing β . The value of Z falls between 0 and 1 ($0 < Z < 1$; 1 is for a perfect grating) and depends on factors such as photosensitivity of the sample and grating contrast ratio.¹⁰ The diffusion length (L_D) can be directly extracted from a linear fit of eq 1, with error bars coming from the fitting procedure (see Supporting Information for details).

This technique measures the change in photoconductivity laterally across the sample, which is associated with the diffusion of photogenerated carriers.^{6,8,14} This measurement geometry is distinct as compared to other methods that measure carrier diffusion through the thickness of the film. Although in a standard solar cell current is extracted in the direction perpendicular to the substrate through the thickness of the film, diffusion in the lateral direction is still strongly correlated to device efficiency for materials whose transport is not strongly anisotropic. For example, a study of halide perovskite thin film devices with grain sizes 100 times larger than the film thickness has shown that grain boundary recombination still plays a role in decreasing solar cell performance, indicating the influence of lateral diffusion.¹⁵

This indicates that the diffusion length measured by SSPG in the lateral geometry is a relevant parameter for solar cell performance. In this work, to confirm that the SSPG technique applied to hybrid perovskites yields a diffusion length similar to that measured by more conventional techniques, we used electron beam induced current (EBIC) to measure the diffusion length of MAPbI₃ and MAPbBr₃ films of the same quality, processing conditions, and lateral sample geometry used for SSPG measurements. The EBIC values agree well with those obtained using SSPG (Figure S8). A full description of the technique including theoretical derivation and error analysis for a wide range of thin-film semiconductors and studies on the effect of laser intensity, electric field, and chopping frequency are the focus of a forthcoming manuscript.

We begin by studying the dependence of diffusion length on the sample preparation method using MAPbI₃. Samples were prepared by depositing thin-film hybrid perovskites on glass substrates by spin-casting from different solvents (details in the Supporting Information). On top of the film, two gold electrodes were deposited (1 mm spacing) for electrical contacts. Figure 2a shows a transform of the change in

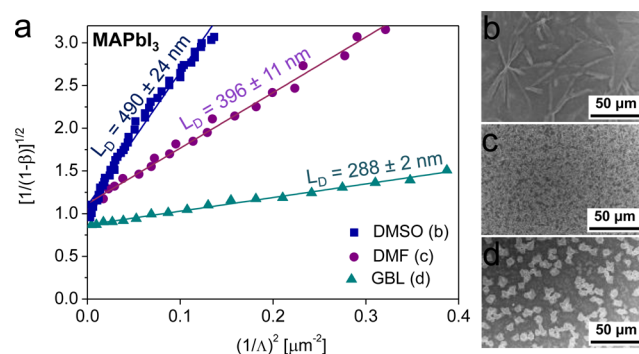


Figure 2. Variation of lateral carrier diffusion length in MAPbI₃. (a) Experimental data of a transform of the photoconductivity ratio (β) as a function of grating size (Λ). The lines are the linear fitting of each corresponding experimental data set. Corresponding scanning electron microscope images of samples prepared with different solvents: (b) DMSO, (c) DMF, and (d) GBL.

conductivity ratio (β) as a function of the grating size (Λ) for MAPbI₃ and the corresponding diffusion lengths for each of the three processing conditions. The film processed with dimethyl sulfoxide (DMSO) solvent yielded the longest diffusion length (up to 490 nm) followed by the dimethylformamide (DMF, up to 396 nm) and γ -butyrolactone (GBL, up to 288 nm) films. The SEM images show morphological differences consistent with the measured diffusion lengths: films cast from DMSO formed large, smooth plates, while films from DMF were continuous but had a higher roughness, and those cast from GBL had the highest porosity (Figure 2b–d). A variety of different processing treatments including solution filtration before spin coating and toluene antisolvent dripping also were tested and showed distinct differences in diffusion length (more detail in Figure S1a). The diffusion length values we measure are similar to what has been reported using other techniques including intensity modulated photocurrent/photovoltage spectroscopy (IMPS/IMVS), photoluminescence quenching, and photoluminescence lifetime combined with mobility, where values of 100–1000 nm are typical, depending on preparation conditions.^{6,8,14}

To gain more insight into the origins of the observed morphology that is created by the solvent, we analyze X-ray diffraction patterns of six MAPbI₃ films processed from DMSO, DMF, and GBL, each with two different preparation conditions (Figure S1b). All films show a perovskite structure with a tetragonal phase/*P4mm* ($a = b = 8.86 \text{ \AA}$, $c = 12.67 \text{ \AA}$) typical of literature reports for MAPbI₃.^{7,16} We observed a direct correlation between diffusion length and the broadening of the XRD peak (Figure S1c–e), which could arise from effects such as smaller crystallite size or microstrain within the film.¹⁷ Assuming that the broadening arises entirely from the size of the crystallites, the full width at half-maximum of the peak corresponding to the (220) crystal orientation was used to estimate the crystallite size in the six MAPbI₃ films with different sample preparation conditions (Supporting Information for details). The diffusion length increased by more than a factor of 2 (from 216 to 490 nm) with an increase in estimated crystallite size from 78 to 152 nm.

In addition to looking at solvent and preparation effects on diffusion length in the pure iodide, we have also examined how the diffusion length varies with halide composition. Here samples based on neat and mixed MAPbI₃ and MAPbBr₃ (hereafter denoted as MAPb(I_{1-x}Br_x)₃) are studied. The mixed MAPb(I_{1-x}Br_x)₃ is of interest because its bandgap can be tuned throughout the region of interest for multijunction solar cells and visible light-emitting diodes or lasers,^{2,4,18–22} although there are currently some problems with spontaneous phase separation under solar illumination.²³ We soaked the samples under laser illumination before the SSPG measurement in order to stabilize the properties (see methods). Spin coating from the mixed halide solutions was used to prepare these alloy samples (see methods). The bandgap gradually becomes larger by adding MAPbBr₃ into the neat MAPbI₃, as can be seen from the gradual blue-shifted absorption with a clear onset following a linear relation $E_G = 0.69[\text{Br}] + 1.55$; where E_G is the optical bandgap (eV) and [Br] is the MAPbBr₃ fraction relative to MAPbI₃, from 0 to 1 (Figure S2a,b). At the same time, there is also a transition from the tetragonal phase to the cubic phase, as shown by the evolution of the tetragonal phase (110) peak into the cubic phase (100) peak, by adding MAPbBr₃ into the neat MAPbI₃ based on X-ray diffraction analysis² (Figure S2c,d). There is only one single phase observed across the transition from tetragonal to cubic phase implying a successful incorporation of iodide–bromide ions into the perovskite structures.

The plot in Figure 3a shows that the MAPbI₃ film has a diffusion length (475 nm) about two times longer than that of the MAPbBr₃ film (201 nm), as indicated by its steeper slope. All alloy compositions initially exhibit diffusion lengths below those of both pure MAPbBr₃ and MAPbI₃ (Figure 3b), consistent with an earlier proposal of trap-state formation in the mixed halide perovskites.²³ Interestingly, after aging the films for 1 month (stored in air at room temperature in the dark) all mixed halide films show a substantial increase in diffusion length from initial values of 151–183 nm to final values of 238–392 nm (Figure 3b and Figure S3). The diffusion length in aged alloy films increases proportionally with the Br fraction up to 0.66 (at 1.97 eV band gap) before dropping to values very close to those seen in the pure bromide film. The pure bromide film showed no change in diffusion length with aging, while the pure iodide film showed a large decrease in diffusion length after one month. This result is consistent with the XRD, which showed partial decomposition to lead iodide only for the pure

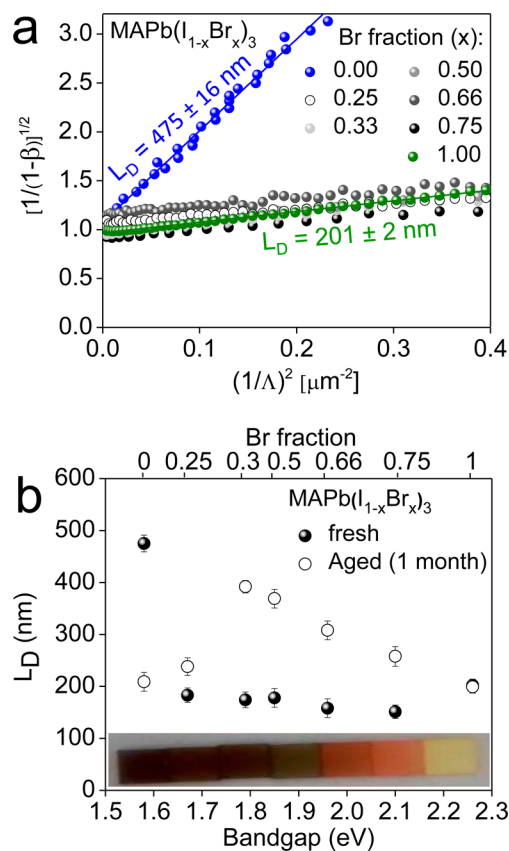


Figure 3. Diffusion length and aging effects in MAPb(I_{1-x}Br_x)₃. (a) Experimental data of a transform of the photoconductivity ratio (β) as a function of grating size (Λ) before aging. The lines are the linear fitting of data from each corresponding composition (the fitting lines and diffusion length for mixed samples are not displayed for clarity). (b) Diffusion length as a function of (initial) bandgap and bromide fraction: fresh samples (filled circle) and aged samples (open circle); inset: photograph of aged samples arranged with their corresponding bandgap.

iodide perovskite; the pure bromide and mixed halide perovskite films showed no crystalline secondary phases (Figure S2c). The only change in the alloy perovskite films with aging was a slight blue shift in the absorption onset (Figure S2a,b), consistent with a previous report.²⁰

The origin of increased diffusion length with aging for mixed halide perovskite films is still unclear, but reactive oxygen species have been reported to play a role in deactivating defect states in the mixed halide perovskites.^{24,25} This strong difference in stability with variation in composition underlines the importance of having a simple and rapid technique for directly measuring the diffusion length of the perovskite itself, isolating its aging characteristics from those of the interfacial and contact layers used in complete devices.

Although the experiment creates an optical grating throughout the entire perovskite film thickness, a transfer-matrix calculation^{26,27} shows that the highest photocarrier generation rate occurs at the surface of the film (Figure S5). This suggests that the SSPG technique could be sensitive to surface recombination and surface passivation effects.²⁸ Figure 4 shows the transform of the photoconductivity ratio as a function of grating size of MAPbI₃ and MAPbBr₃ films before and after coating with a 4 nm thin amorphous aluminum oxide (Al₂O₃) layer deposited by atomic layer deposition (ALD). The

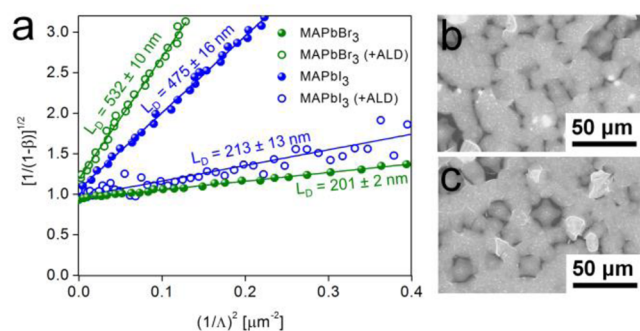


Figure 4. Surface passivation effect on the lateral diffusion length. (a) Experimental data of a transform of the photoconductivity ratio (β) as a function of grating size (λ) before and after passivation with 4 nm thin aluminum oxide film deposited by atomic layer deposition (ALD); the lines are the linear fitting of each corresponding data. Scanning electron microscope images of MAPbBr₃ before (b) and after (c) ALD; the bright-small dots are from sputtered chromium particles.

deposition takes place at 100 °C using trimethylaluminum (TMA) and water (H₂O) as the Al₂O₃ precursors and the whole process takes 30 min (50 cycles). There is a dramatic increase in diffusion length for the MAPbBr₃ film from 201 to 532 nm, while the diffusion length of the MAPbI₃ film decreases from 475 to 213 nm. From XRD it is clear that MAPbI₃ decomposes substantially, as indicated by the appearance of PbI₂ precursor peaks (Figure S6) after the ALD deposition. In fact, we observed that the MAPbI₃ had started to decompose even after 10 cycles of ALD (<1 nm). This can explain both the lower diffusion length and poor signal-to-noise ratio in the measurement. In contrast, the cubic phase of MAPbBr₃ is still preserved without any trace of precursor peaks observed (Figure S6).

To elucidate if surface passivation is the main reason for the diffusion length improvement, we conducted a vacuum annealing experiment by placing a MAPbBr₃ film in the ALD chamber in which all parameters were set to be the same (100 °C, 30 min, 10⁻³ mbar), only without feeding in the precursors. We observed the diffusion length also increased after the vacuum annealing, but only by about 20% from its initial value, which cannot account for the nearly threefold increase seen after ALD (Figure S7). Previously a thin ALD alumina layer has been shown to be an effective passivation scheme for a variety of semiconductor surfaces (Si,²⁹ CIGS,³⁰ ZnO³¹) either through a field effect (fixed interfacial charges) or reduced interfacial trap state density, both of which reduce the surface recombination velocity. However, the exact role of the ALD passivation on hybrid perovskites is still under investigation. As ALD has been used in the past as an encapsulation layer to improve the stability of metal nanowire transparent electrodes,³² we expect it could also serve a similar role here.

To summarize, we have performed a simple and rapid technique to screen quantitatively the diffusion length in hybrid perovskite thin films. This laser grating technique directly measures the diffusion length, which eliminates the need to measure lifetime and mobility separately. We demonstrate that the diffusion length in MAPbI₃ films can be improved from 216 to 490 nm by changing the deposition conditions. We also show that the diffusion length in mixed MAPb(I_{1-x}Br_x)₃ films has a complex aging behavior that varies dramatically with composition: pure iodide films degrade, pure bromide films do not change, and the alloy films improve with aging. Finally, we

demonstrate an improvement in the diffusion length of MAPbBr₃ films from 201 to 532 nm after deposition of a 4 nm thin Al₂O₃ layer by ALD. This remarkable improvement in diffusion length justifies further investigations on interfacial modification with other oxides such as nickel oxide (NiO_x), molybdenum oxide (MoO_x), and titanium oxide (TiO_x) for broadening its applicability not only for solar cells but also for photoelectrochemical water splitting.

■ ASSOCIATED CONTENT

Supporting Information

The Supporting Information is available free of charge on the ACS Publications website at DOI: 10.1021/acs.chemmater.6b00466.

Sample preparation, atomic layer deposition, laser grating setup, X-ray diffraction, transfer matrix modeling, error analysis, electron beam induced current measurements, and data analysis (PDF)

■ AUTHOR INFORMATION

Corresponding Author

*(E.C.G.) E-mail: e.garnett@amolf.nl.

Notes

The authors declare no competing financial interest.

■ ACKNOWLEDGMENTS

The authors thank Dr. Bruno Ehrlér for comments on the manuscript, Haralds Abolins for discussion and suggestions for thin film deposition protocols, Dibyashree Koushik for cross-checking the XRD data, Andries Lof, Parisa Khoram, and Dr. Sophie Meuret for help and discussions regarding the EBIC measurements, and Ricardo Struik for the schematic drawn in Figure 1a. This work is part of the research program of the Foundation for Fundamental Research on Matter (FOM), which is part of The Netherlands Organization for Scientific Research (NWO). L.W.V. and R.E.I.S. acknowledge Nano-nextNL (Project 02A.03), a micro- and nanotechnology consortium of the government of The Netherlands and 130 partners. G.W.P.A., S.B., and E.C.G. acknowledge financial support from the European Research Council under the European Union's Seventh Framework Programme (FP/2007-2013)/ERC Grant Agreement no. 337328, "NanoEnabledPV", and from an industrial partnership between Philips and FOM.

■ REFERENCES

- Lee, M. M.; Teuscher, J.; Miyasaka, T.; Murakami, T. N.; Snaith, H. J. Efficient hybrid solar cells based on meso-structured organometal halide perovskites. *Science* **2012**, *338*, 643–647.
- Noh, J. H.; Im, S. H.; Hoe, J. H.; Mandal, T. N.; Seok, S. I. Chemical management for colorful, efficient, and stable inorganic-organic hybrid nanostructured solar cells. *Nano Lett.* **2013**, *13*, 1764–1769.
- Jeon, N. J.; Noh, J. H.; Yang, W. S.; Kim, Y. C.; Ryu, S.; Seo, J.; Seok, S. I. Compositional engineering of perovskite materials for high-performance solar cells. *Nature* **2015**, *517*, 476–480.
- Zhu, H.; Fu, Y.; Meng, F.; Wu, X.; Gong, Z.; Ding, Q.; Gustafsson, M. V.; Trinh, M. T.; Jin, S.; Zhu, X.-Y. Lead halide perovskite nanowire lasers with low lasing thresholds and high quality factors. *Nat. Mater.* **2015**, *14*, 636–642.
- Burschka, J.; Pellet, N.; Moon, S.-J.; Humphry-Baker, R.; Gao, P.; Nazeeruddin, M. K.; Grätzel, M. Sequential deposition as a route to high-performance perovskite-sensitized solar cells. *Nature* **2013**, *499*, 316–319.

- (6) Stranks, S. D.; Eperon, G. E.; Grancini, G.; Menelaou, C.; Alcocer, M. J. P.; Leijtens, T.; Herz, L. M.; Petrozza, A.; Snaith, H. J. Electron-hole diffusion lengths exceeding 1 micrometer in an organometal trihalide perovskite absorber. *Science* **2013**, *342*, 341–344.
- (7) Jeon, N. J.; Noh, J. H.; Kim, Y. C.; Yang, W. S.; Ryu, S.; Seok, S. I. Solvent engineering for high-performance inorganic-organic hybrid perovskite solar cells. *Nat. Mater.* **2014**, *13*, 897–903.
- (8) Xing, G.; Mathews, N.; Sun, S.; Lim, S. S.; Lam, Y. M.; Gratzel, M.; Mhaisalkar, S.; Sum, T. C. Long-range balanced electron-and hole-transport lengths in organic-inorganic $\text{CH}_3\text{NH}_3\text{PbI}_3$. *Science* **2013**, *342*, 344–347.
- (9) Komuro, S.; Aoyagi, Y.; Segawa, Y.; Namba, S.; Masuyama, A.; Okamoto, H.; Hamakawa, Y. Study of optically induced degradation of conductivity in hydrogenated amorphous silicon by transient grating method. *Appl. Phys. Lett.* **1983**, *42*, 807–809.
- (10) Ritter, D.; Zeldov, E.; Weiser, K. Steady-state photocarrier grating technique for diffusion length measurement in photoconductive insulators. *Appl. Phys. Lett.* **1986**, *49*, 791–793.
- (11) Balberg, I.; Delahoy, A. E.; Weakliem, H. A. Self-consistency and self-sufficiency of the photocarrier grating technique. *Appl. Phys. Lett.* **1988**, *53*, 992–994.
- (12) Nicholson, J. P. Fresnel corrections to measurements of ambipolar diffusion length. *J. Appl. Phys.* **2000**, *88*, 4693–4696.
- (13) Hattori, K.; Okamoto, H.; Hamakawa, Y. Theory of the steady-state-photocarrier-grating technique for obtaining accurate diffusion-length measurements in amorphous silicon. *Phys. Rev. B: Condens. Matter Mater. Phys.* **1992**, *45*, 1126–1138.
- (14) Hoe, J. H.; Song, D. H.; Han, H. J.; Kim, S. Y.; Kim, D.; Kim, H.; Shin, T. K.; Ahn, T. K.; Wolf, C.; Lee, T.-W.; Im, S. H. Planar $\text{CH}_3\text{NH}_3\text{PbI}_3$ Perovskite Solar Cells with Constant 17.2% Average Power Conversion Efficiency Irrespective of the Scan Rate. *Adv. Mater.* **2015**, *27*, 3424–3430.
- (15) Yang, Y.; Yan, Y.; Yang, M.; Choi, S.; Zhu, K.; Luther, J. M.; Beard, M. C. Low surface recombination velocity in solution-grown $\text{CH}_3\text{NH}_3\text{PbBr}_3$ perovskite single crystal. *Nat. Commun.* **2015**, *6*, 7961.
- (16) Quarti, C.; Mosconi, E.; Ball, J. M.; D’Innocenzo, V.; Tao, C.; Pathak, S.; Snaith, H. J.; Petrozza, A.; De Angelis, F. Structural and optical properties of methylammonium lead iodide across the tetragonal to cubic phase transition: implications for perovskite solar cells. *Energy Environ. Sci.* **2016**, *9*, 155–163.
- (17) Suryanarayana, C.; Norton, M. G. *X-ray diffraction: a practical approach*; Plenum Press: New York, 1998.
- (18) White, T. P.; Lal, N. N.; Catchpole, K. R. Tandem solar cells based on high-efficiency c-Si bottom cells: top cell requirements for > 30% efficiency. *IEEE J. Photovolt.* **2014**, *4*, 208–214.
- (19) Gil-Escrig, L.; Miquel-Sempere, A.; Sessolo, M.; Bolink, H. J. Mixed iodide-bromide methylammonium lead perovskite-based diodes for light emission and photovoltaics. *J. Phys. Chem. Lett.* **2015**, *6*, 3743–3748.
- (20) Sadhanala, A.; Deschler, F.; Thomas, T. H.; Dutton, S. E.; Goedel, K. C.; Hanusch, F. C.; Lai, M. L.; Steiner, U.; Bein, T.; Docampo, P.; Cahen, D.; Friend, R. H. Preparation of single-phase films of $\text{CH}_3\text{NH}_3\text{Pb}(\text{I}_{1-x}\text{Br}_x)_3$ with sharp optical band edges. *J. Phys. Chem. Lett.* **2014**, *5*, 2501–2505.
- (21) Kulkarni, S. A.; Baikie, T.; Boix, P. P.; Yantara, N.; Mathews, N.; Mhaisalkar, S. Band-gap tuning of lead halide perovskites using a sequential deposition process. *J. Mater. Chem. A* **2014**, *2*, 9221–9225.
- (22) Cho, H.; Jeong, S.-H.; Park, M.-H.; Kim, Y.-H.; Wolf, C.; Lee, C.-L.; Heo, J. H.; Sadhanala, A.; Myoung, N.; Yoo, S.; Im, S. H.; Friend, R. H.; Lee, T.-W. Overcoming the electroluminescence efficiency limitations of perovskite light-emitting diodes. *Science* **2015**, *350*, 1222–1225.
- (23) Hoke, E. T.; Slotcavage, D. J.; Dohner, E. R.; Bowring, A. R.; Karunadasa, H. I.; McGehee, M. D. Reversible photo-induced trap formation in mixed-halide hybrid perovskites for photovoltaics. *Chem. Sci.* **2015**, *6*, 613–617.
- (24) Tian, Y.; Peter, M.; Unger, E.; Abdellah, M.; Zheng, K.; Pullerits, T.; Yartsev, A.; Sundstrom, V.; Scheblykin, I. G. Mechanistic insights into perovskite photoluminescence enhancement: Light curing with oxygen can boost yield thousandfold. *Phys. Chem. Chem. Phys.* **2015**, *17*, 24978–24987.
- (25) Galisteo-Lopez, J. F.; Anaya, M.; Calvo, M. E.; Miguez, H. Environmental effects on the photophysics of organic-inorganic halide perovskites. *J. Phys. Chem. Lett.* **2015**, *6*, 2200–2205.
- (26) Peumans, P.; Yakimov, A.; Forrest, S. R. Small molecular weight organic thin-film photodetectors and solar cells. *J. Appl. Phys.* **2003**, *93*, 3693–3723.
- (27) Burkhard, G. F.; Hoke, E. T.; McGehee, M. D. Accounting for interference, scattering, and electrode absorption to make accurate internal quantum efficiency measurement in organic and other thin solar cells. *Adv. Mater.* **2010**, *22*, 3293–3297.
- (28) Haridim, M.; Weiser, K.; Mell, H. Use of the steady-state photocarrier-grating technique for the study of the surface recombination velocity of photocarriers and the homogeneity of hydrogenated amorphous silicon films. *Philos. Mag. B* **1993**, *67*, 171–180.
- (29) Kato, S.; Kurokawa, Y.; Miyajima, S.; Watanabe, Y.; Yamada, A.; Ohta, Y.; Niwa, Y.; Hirota, M. Improvement of carrier diffusion length in silicon nanowire arrays using atomic layer deposition. *Nanoscale Res. Lett.* **2013**, *8*, 361.
- (30) Vermang, B.; Fjallstrom, V.; Gao, X.; Edoff, M. Improved rear surface passivation of $\text{Cu}(\text{In,Ga})\text{Se}_2$ solar cells: a combination of an Al_2O_3 rear surface passivation layer and nanosized local rear point contacts. *IEEE J. Photovolt.* **2014**, *4*, 486–492.
- (31) Law, M.; Greene, L. E.; Radenovic, A.; Kuykendall, T.; Liphardt, J.; Yang, P. $\text{ZnO-Al}_2\text{O}_3$ and ZnO-TiO_2 core-shell nanowire dye-sensitized solar cells. *J. Phys. Chem. B* **2006**, *110*, 22652–22663.
- (32) Hsu, P.-C.; Wu, H.; Carney, T. J.; McDowell, M. T.; Yang, Y.; Garnett, E. C.; Li, M.; Hu, L.; Cui, Y. Passivation coating on electrospun copper nanofibers for stable transparent electrodes. *ACS Nano* **2012**, *6*, 5150–5156.